npj | clean water

www.nature.com/npjcleanwater

ARTICLE OPEN

Check for updates

Ultra-high capacity, multifunctional nanoscale sorbents for PFOA and PFOS treatment

Junseok Lee[1], Changwoo Kim[2], Chen Liu[3], Michael S. Wong[4], Natalie L. Cápiro[5], Kurt D. Pennell[3] and John D. Fortner[1]✉

Here, we describe surface functionalized, superparamagnetic iron oxide nanocrystals (IONCs) for ultra-high PFAS sorption and precise, low energy (magnetic) separation, considering perfluorooctanoic acid (PFOA) and perfluorooctanesulfonic acid (PFOS). As a function of surface coating, sorption capacities described are considerably higher than previous studies using activated carbon, polymers, and unmodified metal/metal oxides, among others. In particular, positively charged polyethyleneimine (PEI) coated IONCs demonstrate extreme sorption capacities for both PFOA and PFOS due to electrostatic and hydrophobic interactions, along with high polymer grafting densities, while remaining stable in water, thus maintaining available surface area. Further, through a newly developed method using a quart crystal microbalance with dissipation (QCM-D), we present real-time, interfacial observations (e.g., sorption kinetics). Through this method, we explore underpinning mechanism(s) for differential PFAS (PFOA vs PFOS) sorption behavior(s), demonstrating that PFAS functional head group strongly influence molecular orientation on/at the sorbent interface. The effects of water chemistry, including pH, ionic composition of water, and natural organic matter on sorption behavior are also evaluated and along with material (treatment) demonstration via bench-scale column studies.

npj Clean Water (2023)6:62 ; https://doi.org/10.1038/s41545-023-00263-9

INTRODUCTION

Perfluoroalkyl and polyfluoroalkyl substances (PFAS) are pollutants of concern due to their long-term persistence in the environment and human health effects. PFAS have been industrially produced and used in numerous products such as fire-fighting foams, carpets, paints, and metal plating for decades, leading to wide spread environmental release[1]. PFAS have been detected in surface, ground, drinking, and waste waters at concentrations ranging from ca. 10 to 2000 ng/L depending on extent of release and distance from source(s)[2–6]. Among various PFAS species, long chain C-F compounds, including perfluorooctanoic acid (PFOA) and perfluorooctanesulfonic acid (PFOS), have been associated with numerous potential adverse health effects[7], and thus pose a risk upon exposure[8]. US EPA has recently revised the health advisory levels at 0.004 parts per trillion (ppt, ng/L) for PFOA, and 0.02 ppt for PFOS, while a number of states have proposed or adopted PFAS regulations with a maximum contaminant level as low as 10 ng/L[9].

Due to their unique physicochemical properties, underpinned by strong carbon-fluorine (C-F) bonds[10], PFAS are highly stable in natural systems and typically recalcitrant to conventional chemical and biological degradation processes. To date, various advanced treatment technologies have been explored to treat PFAS in water, including electrochemical oxidation[11–13], photocatalysis[14,15], sulfate radical-based advanced redox process[16–18], thermal destruction[19], biological treatment[20], and other oxidative and reductive methods[21,22]. Additional processes, such as electron beam[23] and plasma[24,25], have also been applied, with higher energy inputs. While several of these processes show promise to treat a range of PFAS, long(er) chain (and fluorine saturated) PFOA and PFOS remain difficult destroy, with PFOS being the more recalcitrant of the two[26,27].

As an alternative to chemical and/or biological destruction, physical-based separation processes, such as adsorption[28,29] and membrane separation[30,31], can be highly effective to treat PFAS regardless of carbon chain length and head group functionality. Removal of PFAS by various adsorbents, including activated carbon[32,33], carbon nanotubes[34], anion-exchange resins[35,36], polymers[37,38], metals, and/or metal oxides[39–41], have been previously described. To improve removal efficacy, additional treatment processes have been explored to augment physical adsorption, including bubbles/mixing[42], and heat[43]. Further, hybrid composite materials and organic functionalization (modification) have also been demonstrated to enhance sorption performance[44]. Depending on the material, both electrostatic and hydrophobic interaction(s) between PFAS and the adsorbent material surface have been observed to be important[45]. From this perspective, organic–inorganic hybrid nanocomposite materials are a promising class of sorbents, which can offer high surface area(s), and flexible surface coating platforms, with tunable (multi)functional groups, along with responsive cores (e.g., magnetic).

In this study, we demonstrate the ability of surface engineered, superparamagnetic iron oxide nanocrystals (IONCs) to effectively remove the PFOA and PFOS in water, and describe the critical role of organic coating functional groups on sorption behavior. Among all materials evaluated, positively charged polyethyleneimine (PEI) coated IONCs showed ultra-high sorption capacities for both PFOA and PFOS due to favorable molecular interactions and high grafting densities. For these, we further explored the effect of water chemistry, including solution pH, ionic composition and strength, and natural organic matter on sorption performance in addition to bench-scale (sand) column studies. We also present an innovative quartz crystal microbalance with dissipation (QCM-D) method to fundamentally describe interfacial PFAS adsorption

[1]Department of Chemical and Environmental Engineering, Yale University, New Haven, CT 06511, USA. [2]School of Earth Sciences and Environmental Engineering, Gwangju Institute of Science and Technology, Gwangju 61005, Republic of Korea. [3]School of Engineering, Brown University, Providence, RI 02912, USA. [4]Department of Chemical and Biomolecular Engineering, Rice University, Houston, TX 77005, USA. [5]Department of Biological and Environmental Engineering, Cornell University, Ithaca, NY 14850, USA. ✉email: john.fortner@yale.edu

processes in situ and in real time. This new method provides rapid, accurate, and continuous response to system perturbations such as changes in solution chemistry and sorbate composition and concentration. Such an approach allows for a mechanistic understanding of competitive sorption dynamics, including molecular (sorbate) orientation, underpinning bulk behavior observations.

RESULTS AND DISCUSSION

Role of surface coating of nanocrystals on PFAS sorption behavior

TEM micrographs in Supplementary Fig. 1 show as synthesized, monodisperse IONCs, and their size distribution (20.9 ± 1.5 nm, 55.3 m^2/g of core specific surface area). IONC crystalline structure is well matched with magnetite (Fe_3O_4) (JCPDS card #190629) by XRD analysis, which is superparamagnetic in this size range, as reported previously[46]. Superparamagnetic functionality was included as part of the material platform for potential applications in low energy, precise (magnetic) separations from larger volumes and/or as a safety feature with regard to unwanted release. IONCs were subsequently surface functionalized with a series of organic coatings, including branched polyethyleneimine (PEI) with different molecular weights (10 kDa and 25 kDa), cetyltrimethylammonium bromide (CTAB), and oleic acid (OA), all allowing for phase transfer into water, termed here as Fe_3O_4@PEI, Fe_3O_4@CTAB, and Fe_3O_4@OA, respectively. Surface functionalized IONCs were characterized in water by dynamic light scattering (DLS) to measure hydrodynamic diameter and surface zeta potential at pH 7 ± 0.2. As tabulated in Supplementary Fig. 2a, the hydrodynamic diameter is 63.0 ± 2.4 nm for Fe_3O_4@PEI25k, 40.4 ± 2.8 nm for Fe_3O_4@PEI10k, 25.8 ± 3.0 nm for Fe_3O_4@CTAB, and 32.6 ± 3.6 nm for Fe_3O_4@OA. Zeta potential of Fe_3O_4@PEI25k, Fe_3O_4@PEI10k, Fe_3O_4@CTAB, and Fe_3O_4@OA is 54.3 ± 1.3, 57.4 ± 1.5, 29.1 ± 4.9, and −24.2 ± 1.8 mV, respectively (Supplementary Fig. 2b). Coating analysis, including grafting densities and composition are presented in Supplementary Table 1.

Batch surface coating-dependent PFAS sorption tests were performed at pH 7 ± 0.2. As shown in Fig. 1, positively charged Fe_3O_4@PEI nanocrystals (NCs) demonstrate significantly higher sorption density compared to negatively charged Fe_3O_4@OA NCs. The maximum sorption capacity of PFOA and PFOS was 18.3 mmol PFOA g^{-1} NC and 88.8 mmol PFOS g^{-1} NC for Fe_3O_4@PEI25k, and 11.9 mmol PFOA g^{-1} NC and 83.5 mmol PFOS g^{-1} NC for Fe_3O_4@PEI10k, respectively. Negatively charged Fe_3O_4@OA have significantly lower sorption capacities for both PFOA and PFOS (1.83 mmol PFOA g^{-1} NC and 6.58 mmol PFOS g^{-1} NC). As highlighted in Table 1, Fe_3O_4@PEI materials described in this study demonstrate some of the highest sorption capacities reported to date. This is not only due to a high number (related to PEI amine density, Supplementary Table 1) of favorable amine–anion (PFAS) head group interactions per particle[47,48], but also a function of high particle (aqueous) stability, thus maximum surface area/site availability (Supplementary Fig. 2). Comparatively, Fe_3O_4@PEI25k is observed to have higher sorption capacities than Fe_3O_4@PEI10k despite having a similar number of amine groups. This is likely due to a combination of relatively higher grafting (mass) density of PEI25k and a higher amine to carbon ratio compared to PEI10k.

All batch sorption isotherms were well matched with a Langmuir adsorption model (Supplementary Table 2) with the corresponding sorption constant (k) for PFOA calculated to be much higher than that of PFOS regardless of sorbent. Further, for comparison, we also modeled sorption data with a Freundlich isotherm as well (Supplementary Table 2). Interestingly, PFOS is observed to have higher maximum sorption density (Q_{max}) compared to PFOA, for all material combinations explored. For example, the k and Q_{max} values on Fe_3O_4@PEI25k are 657 L/mmol and 18.3 mmol/g for PFOA, and 4.22 L/mmol and 88.8 mmol/g for PFOS, respectively. This difference indicates that PFAS functional head group(s) contribute to the sorption behavior as PFOA and PFOS having similar fluorine saturated tail structures. With regard to functional group acidity, PFOS, has a lower pKa value (<0) than PFOA (0.5–3.8), in addition to higher affinity for octanol (a model non-aqueous phase, log $K_{OW} = 5.43$) compared to PFOA (log $K_{OW} = 5.11$)[49–52]. As discussed by others, amine–sulfonic interactions typically have a more negative enthalpy (ΔH) value (−42.81 kJ/mol) compared to amine–carboxyl interactions (−21.41 kJ/mol), which also likely contributes to (more) favorable adsorption[53,54]. These property differences may also impact association sterics, in terms of average geometrical orientation of the sorption event, which is further explored and discussed below.

Real-time analysis of PFAS sorption via QCM-D

To better understand fundamental sorption dynamics, a quartz crystal microbalance with dissipation (QCM-D) monitoring technique was developed to observe real time, in situ sorption behavior of PFAS. For this, we arrange a stable, monolayer of IONCs at the sensor interface—whereby varied aqueous solutions can be introduced sequentially and equilibrated, including changes in water chemistry and PFAS concentration/type (Supplementary Fig. 3). Supplementary Fig. 4 shows the kinetics (slope of frequency shift) of IONC deposition and sensor surface saturation (i.e., monolayer coverage) at or above 5 mg/L of concentration of NCs. Once stabilized IONCs demonstrate relative fast responses upon introducing PFAS solutions and reached equilibrium within minutes. These results are consistent with the batch sorption isotherm and kinetic tests for both PFOA and PFOS using IONCs (Supplementary Fig. 5). To further understand PFAS sorption kinetics on IONCs, the slope of the frequency shift (f_{slope}) was calculated from the data obtained during QCM-D sorption experiments. Since the frequency shift (Δf) is proportional to a change in mass (Δm) on the crystal surface, the rate of Δf change is equivalent to the rate of mass change on the crystal surface (i.e., the rate of PFAS attachment or release)[55,56]. Hence, the PFAS sorption rate (kinetics) can be determined by calculating the slope of frequency shift (f_{slope}). As shown in Supplementary Fig. 6, Fe_3O_4@CTAB NCs showed the highest value of f_{slope}, followed by Fe_3O_4@PEI10k and Fe_3O_4@PEI25k, which is inversely proportional to the hydrodynamic diameter of IONCs. We expected the thicker PEI (and denser) surface coating layer requires more time for PFAS to fully sorb, which is likely due to mass transfer limitations, while showing overall higher sorption densities due to relatively more binding sites.

Based on both frequency shifts from flowing IONCs and PFAS solutions to Q-sensor, we determined both PFOA and PFOS sorption density of IONCs using deposited mass via the Sauerbrey equation[57]. We confirmed no PFAS was directly attached to quartz crystal sensor without IONCs (Supplementary Fig. 7), thus any observed frequency shift in the presence of PFAS is due to its association with IONCs. Supplementary Fig. 8 details sorption isotherms for both PFOA and PFOS for IONCs with different surface coatings (PEI25k, PEI10k, and CTAB) as calculated by mass per IONC (mass) via QCM-D. The initial calculated sorption density obtained from QCM-D showed relatively lower values than those from batch sorption tests. Based on our previous research, frequency shifts can be observed with the release of sorbed water associated with certain polymers, thus complicating sorbate association measurements[58]. To address this issue, we developed a correction factor based on calculated mass of water associated with IONCs. In Fig. 2, we present PFAS sorption isotherms on IONCs determined by both batch sorption and QCM-D methods with

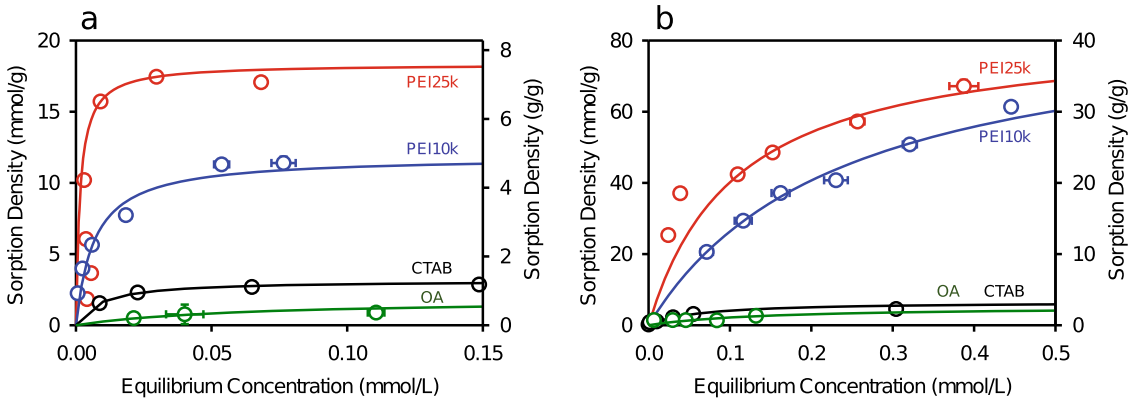

Fig. 1 Batch PFAS sorption isotherms. Comparing **a** PFOA and **b** PFOS sorption on iron oxide nanocrystals (IONCs) with different organic (surface) coatings: positively charged PEI (25k and 10k of MW) and CTAB, and negatively charged OA. All experiments were performed at pH 7.

Table 1. Summary of adsorption capacities for PFAS on various adsorbents.

Adsorbate	Adsorbent	Water matrix	pH	Adsorption capacity		Ref.
				mg/g	mmol/g	
PFOA	PAC	DI water	3	426	1.03	69
	GAC	DI water	5	476	1.15	70
	Polyacrylonitrile fiber-derived activated carbon fibers (PACFs)	DI water	5	302	0.73	71
	SWCNT	DI water	6	80	0.19	72
	Modified titanate nanotubes	DI water	2–10	1100	2.66	61
	Anion Exchange Resin (IRA910)	DI water	6	1440	3.47	59
	Anion Exchange Resin (IRA400)	DI water	2–12	1210	2.92	73
	Polyaniline nanotubes (PANTs)	DI water	2–9	1100	2.66	74
	Quaternized Cotton	DI water	3–10	1240	2.99	75
	Aminated rice husk	DI water	5	1030	2.49	76
	MOF	DI water	5	500	1.2	77
	Magnetite NPs	DI water	7	62.5	0.15	78
	Fe_3O_4@PEI25k (Our work)	DI water	7	7580	18.3	
PFOS	PAC	DI water	3	440	0.88	69
	GAC	DI water	5	1160	2.32	70
	Polyacrylonitrile fiber-derived activated carbon fibers (PACFs)	DI water	5	760	1.52	71
	SWCNT	DI water	6	560	1.12	72
	SWCNT	DI water		710	1.42	79
	Polyaniline nanotubes (PANTs)	DI water	2–9	1650	3.30	74
	Anion Exchange Resin (IRA67)	Actual WW	3	2750	5.5	80
	Anion Exchange Resin (IRA67)	DI water	3	2500	5.0	81
	Aminated polyacrylonitrile fibers (APANFs)	DI water	3	7500	15.0	42
	Chitosan-based molecularly imprinted polymer (MIP)	DI water	3–10	1460	3.53	82
	Crosslinked Chitosan	DI water	3	2500	6.04	83
	Quaternized Cotton	DI water	3–10	1750	3.50	75
	Aminated rice husk	DI water	5	1330	2.65	76
	Porous aromatic framework (PAF-45)	DI water	3	5850	11.7	84
	Magnetic fluorinated vermiculite	DI water	6	1130	2.26	41
	Fe_3O_4@PEI25k (Our work)	DI water	7	44,410	88.8	

PAC powdered activated carbon, *GAC* granular activated carbon, *SWCNT* single-walled carbon nanotubes, *MOF* metal organic framework, *NPs* nanoparticles, *WW* wastewater.

such correction factors. Overall, corrected sorption data from QCM-D (dotted line) experiments are similar to batch sorption trends and values, which highlights QCM-D as a powerful tool to quantify and compare relative sorption behavior(s) in real time.

Competitive sorption of PFAS: multi-sorbate system

Multi-sorbate tests considering both PFOA and PFOS were performed to determine competitive effects on sorption isotherm behavior(s) using Fe_3O_4@PEI25k NCs (highest performing material).

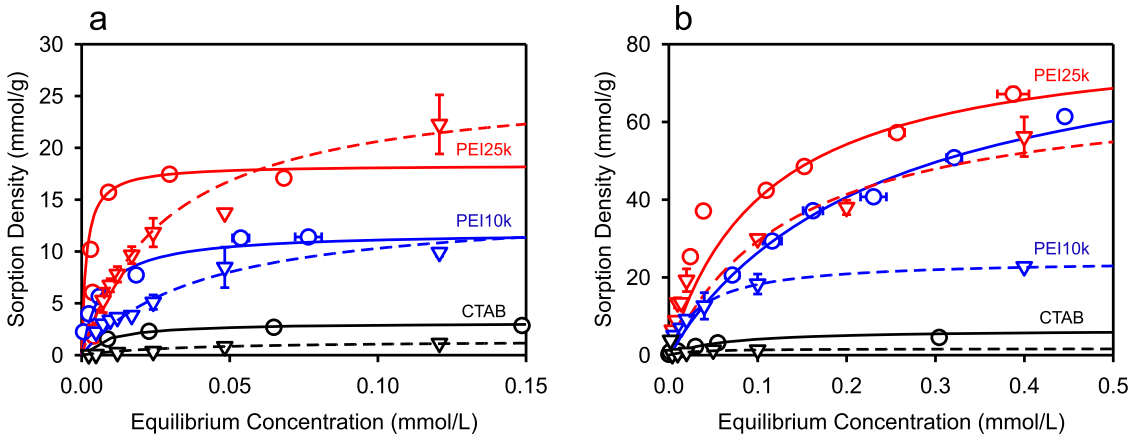

Fig. 2 Comparing batch PFAS sorption isotherms with QCM-D sorption results. a PFOA and **b** PFOS obtained via batch (circle dot and solid line) and QCM-D (reverse triangle dot and dotted line) methods. Data for batch sorption is replotted from Fig. 1 for direct comparison. QCM-D results are obtained by multiplying QCM-D correction factor with sorption density.

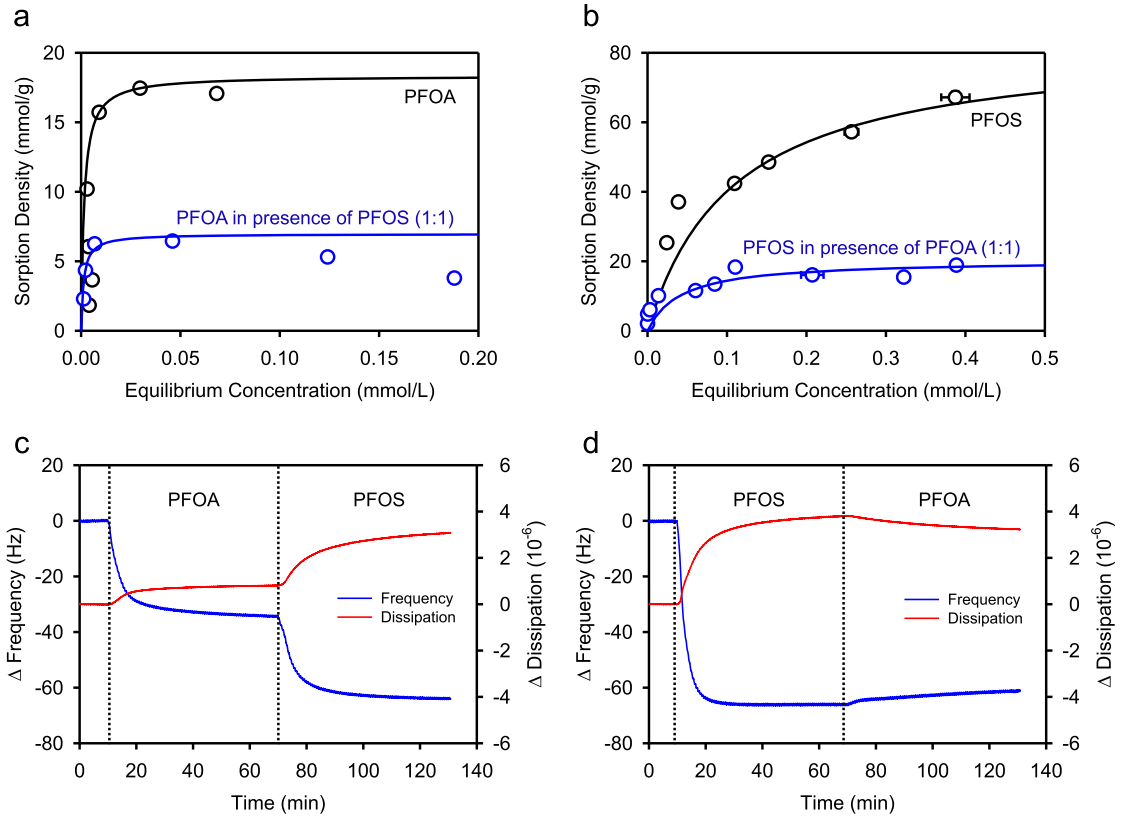

Fig. 3 Understanding competitive PFAS (PFOA vs. PFOS) sorption dynamics. Single- and multi-sorption isotherms on PEI coated IONCs for **a** PFOA and **b** PFOS single-sorbate systems (black line) and multi-sorbate systems (PFOA and PFOS (blue line)). Multi-sorption tests were performed with the same initial concentration of both PFOA and PFOS from 0.02 to 0.1 mmol/L at pH 7. **c**, **d** Time dependent frequency and dissipation shifts (overtone $n = 3$) of the IONCs coated Q-sensor with introducing both PFOA and PFOS sequentially, and vice versa, by QCM-D analysis.

Sorption isotherms for multi-sorbate systems (both PFOA and PFOS with a molar ratio of 1:1) and single-sorbate are presented in Fig. 3a, b. For these conditions, we observed PFOA sorption was significantly hindered in the presence of PFOS, for which maximum sorption capacity was 18.3 mmol g^{-1} (PFOA as the single sorbate) and 7.0 mmol g^{-1} for multi-sorbate systems, respectively. The sorption density for PFOS was also considerably decreased in the presence of PFOA (88.8 mmol g^{-1} for single (PFOS as single sorbate) and 20.4 mmol g^{-1} for multi-sorbate systems, respectively). For both, sorption capacities in multi-sorbate system were lower than that of single-sorbate test, which is likely due to not only differences in free energy of association, but also steric hindrance(s), among other complicating factors in a competitive, multi-sorbate system[59,60]. Sorption density of PFOA on IONCs in the multi-sorbate system also decreased at higher equilibrium concentrations (above 0.1 mmol/L), indicating that PFOA molecules adsorbed on IONCs are favorably exchanged, to some degree, by PFOS.

To further evaluate sorption preference between PFOA and PFOS, real-time sorption behavior was evaluated using the QCM-D

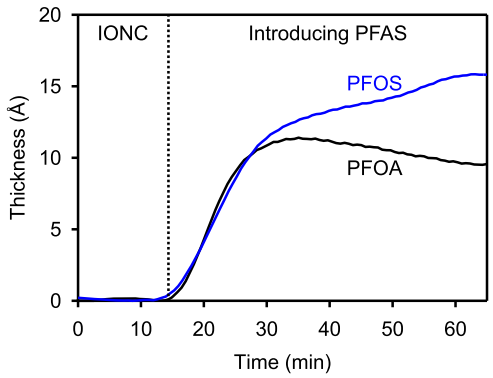

Fig. 4 Comparing sorbed PFAS molecular orientation(s). Thickness of the attached layer of PFOA and PFOS on the IONC coated Q-sensor as calculated by the Voigt model via frequency shift (*f*) and dissipation (*D*) during PFAS sorption.

method described above. To do this, we introduced either 0.6 mmol/L of PFOA or PFOS solutions over IONCs coated Q-sensor sequentially. As shown in Fig. 3c, d, frequency and dissipation shifts associated with PFOA and PFOS sorption events were observed, indicating attachment (sorption) of PFAS on IONCs. After stabilization, we then switched the solutions from PFOA to PFOS and PFOS to PFOA, respectively. We observed additional frequency and dissipation shifts in the system with newly introduced PFOS, indicating molecular exchange and/or additional sorption (Fig. 3c), while no changes in both frequency and/or dissipation were observed when PFOA was introduced to a system with PFOS previously sorbed (Fig. 3d). These observations support batch results, described above, further implicating the key role of the PFAS head group with regard to sorption behavior.

Critical role of functional groups of PFAS on sorption behavior

PFOA with carboxylic head group shows a higher affinity to positively charged IONCs than PFOS, resulting in higher Langmuir adsorption constants (k). In comparison, the sulfonic group of PFOS results in a relatively lower k value due to lower bulk affinity compared PFOA; however, PFOS has three different resonance structure(s) which, when taken together, allows for overall more favorable interactions. To explore this directly, we demonstrated the thickness of PFAS layer, as a function of PFAS type, using the Voigt model via QCM-D analysis. With all variables held constant (IONC, water chemistry, etc.) except for PFAS type, Fig. 4 shows that a difference between PFOA and PFOS sorbed layers is about 5 angstrom (Å), indicating the orientation of sorbed PFAS is different based on the functional head groups. For these, on average PFOS is likely more vertically aligned on the surface of IONCs due to the resonance structure of sulfonic group, while PFOA aligns in a more horizontal fashion (on average), which is also supported by the maximum sorption values observed (i.e., higher sorption density is possible with vertically oriented PFOS). Differences in sorbed orientation between PFOA and PFOS may also contribute to the relative recalcitrance of PFOS relating to steric hindrance and/or active site distance from a reactive material surface(s).

Effect of water chemistry on PFAS sorption behavior

To understand how water chemistry affects PFAS sorption behavior, we evaluated PFAS sorption using Fe_3O_4@PEI25k as a function of solution pH, ionic strength and type, and NOM in water. Figure 5a, b shows that higher sorption densities were observed under both acidic (pH 4.0) and neutral (pH 7.0) conditions, compared to basic conditions (pH 10.0), as expected. The maximum sorption capacity was 14.7 mmol g^{-1} at pH 4.0, 18.3 mmol g^{-1} at pH 7.0, 9.2 mmol g^{-1} at pH 10.0 for PFOA, and 58.8 mmol g^{-1} at pH 4.0, 83.5 mmol g^{-1} at pH 7.0, and 38.5 mmol g^{-1} at pH 10.0 for PFOS, respectively. The observed decrease in sorption at higher pH values was attributed to a decrease in surface zeta potential, and thus, a lower electrostatic affinity for negatively charged PFAS molecules (Supplementary Fig. 9). We also observed a decrease in maximum sorption capacity at lower pH (pH 4) compared to neutral pH (pH 7). As reported by others, acidic conditions can affect PFAS sorption[61]. Here, a net decrease in zeta potential (ca. 14% from pH 7 to pH 4) likely contributes to a lower (maximum) sorption capacity at pH 4.

The effect of ionic strength and type on PFAS sorption was also evaluated using Fe_3O_4@PEI25k NCs via batch sorption experiments at pH 7. Here NaCl, $CaCl_2$, $MgCl_2$, were evaluated along with a synthetic groundwater (SGW) and compared with ultrapure water (UPW). Synthetic groundwater was prepared as described by others[62], and the composition is summarized in Supplementary Table 3. As shown in Fig. 5c, d, sorption capacities for both PFOA and PFOS decreased in the presence of all salts evaluated and the synthetic groundwater. The maximum sorption densities for PFOA were observed to be 18.3, 5.7, 5.1, 5.7, and 14.3 mmol g^{-1} for ultrapure water, NaCl, $CaCl_2$, $MgCl_2$, and synthetic groundwater, respectively, and 83.5, 54.3, 69.0, 73.7, and 31.5 mmol g^{-1} for PFOS for ultrapure water, NaCl, $CaCl_2$, $MgCl_2$, and synthetic groundwater, respectively. We observed competitive effects of ionic species on PFAS sorption performance, with similar or higher hindrance observed for NaCl compared to $CaCl_2$ and $MgCl_2$. This is likely due to the competitive effect(s) of counterions, here as anions, on positively charged IONCs in which concentration of counter ion (Cl^-) in NaCl is higher than divalent cations ($CaCl_2$ and $MgCl_2$) for identical ionic strengths. Despite these interferences, material performance under real-world conditions remains considerably higher than other reported sorbents which only considered pure water (i.e., best case scenario), Table 1. For all suspensions evaluated, no IONC aggregation was observed under any condition evaluated (Supplementary Fig. 10), thus minimizing the loss of surface area as a confounding performance factor.

PFAS sorption capacities also decreased in the presence of NOM (0–0.5 mg/L). To quantify this process, we evaluated the role of humic acid (HA) concentration on sorption density via QCM-D analysis. As shown in Supplementary Fig. 11, sorption densities decreased with increase of HA concentration. HA, with a large cation exchange capacity, readily competes in bulk with positively active sites on IONCs for PFAS sorption, as observed by others for negatively charged pollutants[63,64].

Sequestration of PFOA or PFOS in column studies

To demonstrate application potential, effluent breakthrough curves obtained following the injection of solutions containing PFOA or PFOS into columns packed IONC treated Ottawa sand are shown in Fig. 6. For the PFOA column study, a solution containing 100 µg/L PFOA in 10 mmol/L NaCl was introduced for 10 pore volumes (PVs), with no detectable levels of PFOA observed in effluent samples. To assess the limiting adsorptive capacity of the IONC-treated sand, the influent concentration of PFOA was then increased to 10 mg/L (considered as a very high environmental PFAS concentration), which resulted in detection of PFOA after ~31 PVs. The concentration of PFOA increased steadily to a relative concentration (C/C_0) of 0.83 after 39 PVs, and reached the influent concentration ($C/C_0 = 1$) at 49 PVs (Fig. 6a). Over the course of the experiment, a total of 5.16 mg of PFOA were retained, which corresponds to 5.37 mmol/L PFOA per g of IONC (2.34 mg total IONC in the column), in line with batch sorption study results.

For the PFOS column study, a solution containing 100 µg/L PFOS in 10 mmol/L NaCl was introduced for ~10 PVs with no detectable levels of PFOS observed in the column effluent. Similar to the PFOA column study, the concentration of PFOS in the

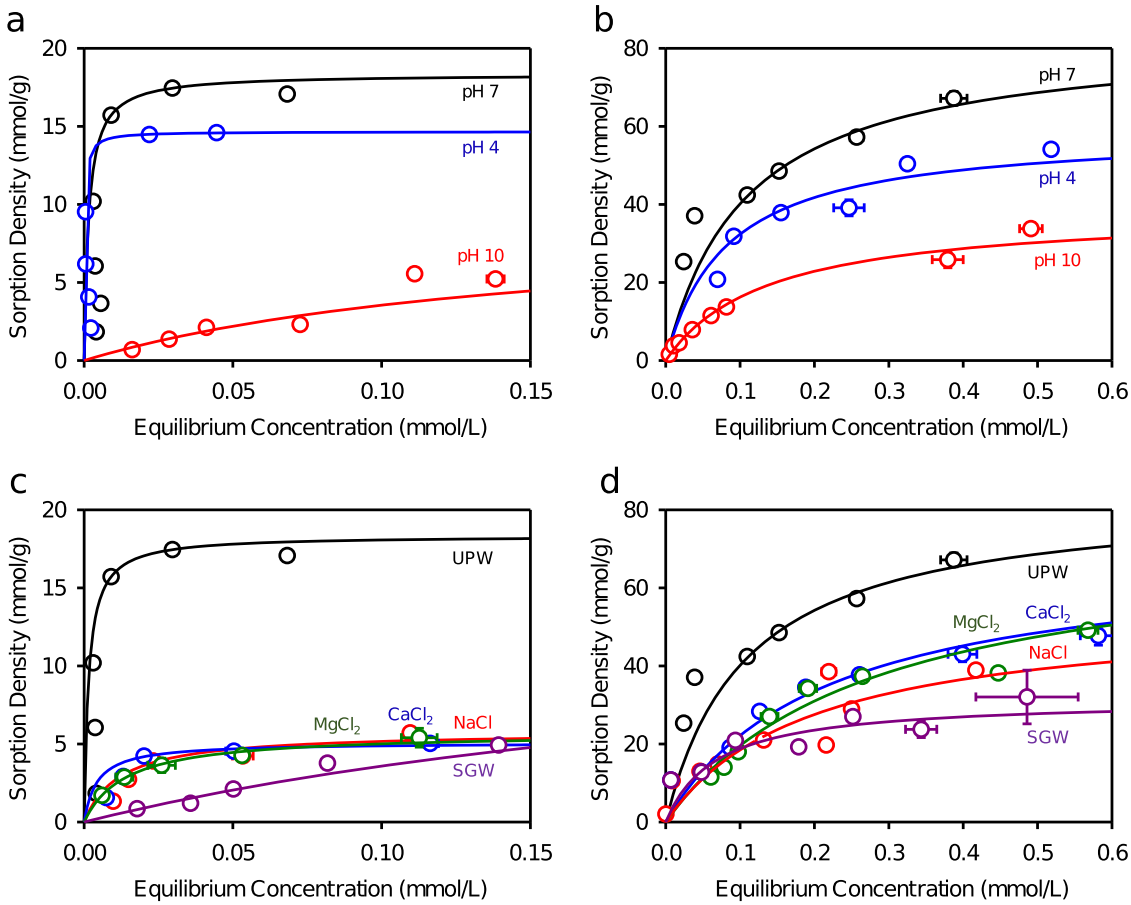

Fig. 5 Quantifying the role(s) of water chemistry. a PFOA and **b** PFOS sorption isotherm on PEI coated IONCs (Fe_3O_4@PEI25k) as a function of pH (4.0 (blue), 7.0 (black), and 10.0 (red)). Sorption isotherm for **c** PFOA and **d** PFOS with different water chemistry of ultrapure water (UPW, black), NaCl (red), $CaCl_2$ (blue), $MgCl_2$ (green), and synthetic groundwater (SGW, purple), respectively. Total ionic strength for all solutions was adjusted to be identical to SGW.

influent solution was then increased to 10 mg/L and PFOS was subsequently detected in the effluent after ~23 PVs, and increased steadily to the influent concentration ($C/C_0 = 1$) after 39 PVs (Fig. 6b). Overall, a total of 6.34 mg of PFOS was retained in the IONC-treated column, which corresponds to 5.18 mmol/L PFOS per g of IONCs (2.45 mg total in the column), also in line with batch studies. When compared to control columns conducted with clean 40–50 mesh Ottawa sand, retention, thus treatment, of PFOA or PFOS in IONC-treated columns increased by more than three orders of magnitude, suggesting potential as a new sorbent material for in situ treatment processes.

METHODS

Preparation of organic (surface) functionalized IONCs

Iron oxide nanocrystals (IONCs) were synthesized by iron precursor decomposition at high temperature as described previously[65]. Synthesized NCs were then functionalized with different organic surfactants using probe sonication via ligand exchange and encapsulation methods[66,67]. Branched PEI, CTAB, and OA were used as surface stabilizers. 0.4 mL of NCs in hexane solution was mixed with particular amounts of surface stabilizer in 5 mL of ultrapure water (18.2 MΩ·cm, Millipore) by applying a probe sonicator (UP50H, Hielscher) at 80% amplitude and full cycle for 10 min. The remaining hexane in solution was removed by putting the solution under the fume hood for 24 h. To remove excess surfactants the solution was filtered by ultrafiltration membrane (cellulose, 100 kDa MWCO, Millipore) with stirring, followed by syringe filtration (0.22 μm PES, Millipore). The concentration of functionalized IONCs in water was measured by inductively coupled plasma mass spectroscopy (ICP-MS, Elan DRC-e, Perkin Elmer).

Sorption isotherms

Engineered IONCs (10 mg/L NC) were tested for PFAS sorption in the range of 0.01 to 0.2 mmol/L of PFOA and 0.01 to 0.6 mmol/L of PFOS concentrations at different pH conditions (4.0, 7.0, and 10.0 ± 0.2). Solution pH was adjusted using HNO_3 and NaOH immediately after initiating sorption test, and further adjusted and/or confirmed again during the course of the experiment (after 4 h). At equilibrium (after 24 h), the NCs were separated using ultracentrifuge (Sorvall WX 80, Thermo Scientific) at 50,000 rpm for 2 h, and the remaining concentrations of PFAS were measured by ultra performance liquid chromatograph (UPLC-MS/MS) (Waters Corporation, Milford, MA). The detailed procedures for PFAS quantification are presented in the Supporting Information. The measured sorption density (mmol of adsorbed PFAS per mass of NCs in the sample) as a function of equilibrium concentration of PFAS (mmol/L) was fitted by both Langmuir and Freundlich sorption isotherms. The Langmuir isotherm was obtained by the following equation:

$$q_e = \frac{q_{max} k C_e}{(1 + k C_e)} \quad (1)$$

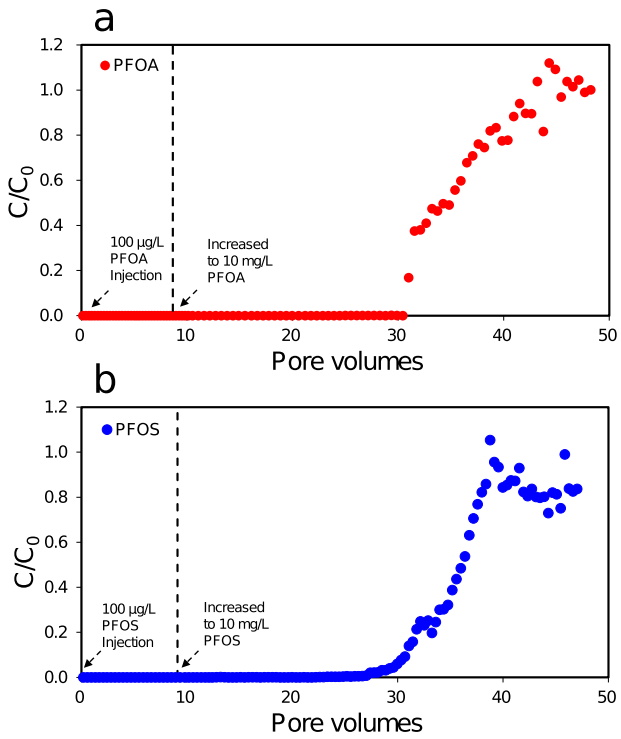

Fig. 6 Bench scale treatment evaluation. Effluent breakthrough curves for **a** PFOA and **b** PFOS in columns packed with IONCs (2.9 mg) treated 40–50 mesh Ottawa Sand (80 g).

where q_e is sorption density at equilibrium (mmol/g), q_{max} is the maximum sorption density, k is Langmuir sorption constant (L/mmol), and C_e is equilibrium concentration of PFAS (mmol/L). And the Freundlich isotherm was determined as follows:

$$q_e = KC_e^{1/n} \tag{2}$$

where K and n are Freundlich sorption constants. Competitive sorption experiments were conducted with the initial concentrations of both PFOA and PFOS from 0.02 to 0.1 mmol/L at pH 7. We adjusted solution pH twice, and other experimental conditions and procedures were identical to the single-sorbate sorption isotherm tests.

Quartz crystal microbalance with dissipation (QCM-D)

We performed quartz crystal microbalance with dissipation (QCM-D, Q-sense E4, Biolin Scientific) measurements by frequency (f) and energy dissipation (D) of silica-coated Q-sensor (QSX-303, Q-sense). The mass deposited on the crystal surface per unit area (Δm) was determined by measuring frequency shift of the crystal using Sauerbrey relationship as described below:

$$\Delta m = -\frac{C}{n}\Delta f_n \tag{3}$$

where C is the crystal constant (17.7 ng/(cm^2·Hz) for 5 MHz quartz crystal), n is the overtone number (1, 3, 5, 7, 9, 11, and 13), and Δf_n is frequency shift at overtone number n. Considering the stability of the instrument, we used third overtone for the analysis of data in this study. For all measurements, we maintained the flowrate of solutions at 0.1 mL/min and the temperature inside the unit at 20.0 °C.

Determination of PFAS sorption behavior via QCM-D study

Real-time frequency shifts were obtained to determine PFAS sorption isotherm on IONCs using QCM-D as following sequence. First, positively charged IONCs (PEI and CTAB coated) were introduced to quartz crystal sensor. We determined the maximum surface NC coverage by evaluating wide range of NC concentrations, as shown in Supplementary Fig. 4. Sensors were saturated with NCs (solution) for 20 min, and subsequently flowed with ultrapure water to stabilize and eliminate any loosely associated NCs to the Q-sensor. After stabilization, we introduced PFAS solutions, which showed additional frequency shifts regard to mass of PFAS attached to the IONCs on sensor. Sorption isotherm is determined from the deposited mass of PFAS and IONCs on the Q-sensor, which calculated from frequency shift through Sauerbrey equation.

QCM-D factor

To compensate the underestimation of sorption capacity in QCM-D measurement due to attachment of water molecules on the Q-sensor, we applied QCM-D correction factor for sorption density. We calculated the QCM-D correction factor as described below.

$$\text{QCM} - \text{D factor} = \frac{\text{Mass of (NCs} + \text{Water)}}{\text{Mass of NCs}} \tag{4}$$

The mass of sorbed water is calculated from the difference of volume between NC core size and hydrodynamic diameter by multiplying density of water.

Thickness of deposited layer on the Q-sensor

The thickness of deposited layer was calculated by analyzing the recorded Δf and ΔD data through Voigt model[68]. The resulting thickness (δ) was obtained by equation as below.

$$\delta = \sqrt{\frac{2\eta_0}{\omega\rho_0}} \tag{5}$$

where η is shear viscosity, ω is angular velocity ($\omega = 2\pi f$), and ρ is density.

Column studies

Column experiments were performed to quantify the adsorption of PFOA or PFOS by IONCs under dynamic flow conditions. A suspension of IONCs (20 mL at 145 mg/L) was mixed with 80 g of 40–50 mesh Ottawa sand and allowed to dry at 60 °C for 48 h. The IONC-treated sand, which contained ~2.9 mg IONC, was then packed into a borosilicate glass column (2.5 cm i.d. × 10 cm length) in 1-cm increments, flushed with CO_2 gas for 1 h, and then saturated with degassed background electrolyte solution (10 mmol/L NaCl) at a flow rate of 1.0 mL/min. The resulting pore volume (PV) of the water-saturated columns was ~20.5 mL. Non-reactive tracer tests were performed after water saturation of each column by injecting 3.5 PVs of 10 mmol/L NaBr followed by 3.5 PVs of 10 mmol/L NaCl using a Chrome Tech P-010 isocratic pump (Apple Valley, MN) at a flow rate of 0.12 mL/min, which corresponds to a pore-water velocity of ~1 m/day. A schematic diagram of the column apparatus is shown in Supplementary Fig. 12.

To assess the ability of the IONC-treated sand to sequester PFOA and PFOS, aqueous solutions containing either PFOA (100 µg/L) or PFOS (100 µg/L) in 10 mmol/L NaCl were injected into the columns at a flow rate of 0.12 mL/min. After ~10 PV, the influent concentration of PFOA or PFOS was increased from 100 µg/L to 10 mg/L to determine to maximum adsorption capacity of the IONCs. Effluent samples were collected continuously using a Spectra/Chrom® CF-2 fraction collector (Spectrum Chemical Mfg. Corp., New Brunswick, NJ) to monitor for PFAS breakthrough. Effluent samples were filtered through 0.45 µm GE Healthcare Whatman™ GD/X Glass Micro Fiber (GMF) syringe filter (GE Healthcare, Chicago, IL) and diluted to an appropriate concentration range prior to analysis using a Waters Xevo™

TQ-S Micro triple quadrupole mass spectrometer (LC–MS/MS) as described in the Supporting Information.

DATA AVAILABILITY

The datasets used and/or analyzed during the current study available from the corresponding author on reasonable request.

Received: 28 February 2023; Accepted: 15 June 2023;
Published online: 05 September 2023

REFERENCES

1. Beesoon, S. & Martin, J. W. Isomer-specific binding affinity of perfluorooctanesulfonate (PFOS) and perfluorooctanoate (PFOA) to serum proteins. *Environ. Sci. Technol.* **49**, 5722–5731 (2015).
2. Bai, X. & Son, Y. Perfluoroalkyl substances (PFAS) in surface water and sediments from two urban watersheds in Nevada, USA. *Sci. Total Environ.* **751**, 141622 (2021).
3. Cordner, A. et al. Guideline levels for PFOA and PFOS in drinking water: the role of scientific uncertainty, risk assessment decisions, and social factors. *J. Expo. Sci. Environ. Epidemiol.* **29**, 157–171 (2019).
4. Hu, X. C. et al. Detection of poly-and perfluoroalkyl substances (PFASs) in US drinking water linked to industrial sites, military fire training areas, and wastewater treatment plants. *Environ. Sci. Technol. Lett.* **3**, 344–350 (2016).
5. Brusseau, M. L., Anderson, R. H. & Guo, B. PFAS concentrations in soils: Background levels versus contaminated sites. *Sci. Total Environ.* **740**, 140017 (2020).
6. Salvatore, D. et al. Presumptive contamination: a new approach to PFAS contamination based on likely sources. *Environ. Sci. Technol. Lett.* **9**, 983–990 (2022).
7. Sunderland, E. M. et al. A review of the pathways of human exposure to poly-and perfluoroalkyl substances (PFASs) and present understanding of health effects. *J. Expo. Sci. Environ. Epidemiol.* **29**, 131–147 (2019).
8. Kwiatkowski, C. F. et al. Scientific basis for managing PFAS as a chemical class. *Environ. Sci. Technol. Lett.* **7**, 532–543 (2020).
9. USEPA. *Drinking Water Health Advisories for PFOA and PFOS* (2022).
10. Banks, R. E., Smart, B. E. & Tatlow, J. *Organofluorine Chemistry: Principles and Commercial Applications* (Springer Science & Business Media, 2013).
11. Huang, D. et al. Amorphous Pd-loaded Ti4O7 electrode for direct anodic destruction of perfluorooctanoic acid. *Environ. Sci. Technol.* **54**, 10954–10963 (2020).
12. Liu, Y. et al. Enhanced perfluorooctanoic acid degradation by electrochemical activation of sulfate solution on B/N codoped diamond. *Environ. Sci. Technol.* **53**, 5195–5201 (2019).
13. Rao, U. et al. Structural dependence of reductive defluorination of linear PFAS compounds in a UV/electrochemical system. *Environ. Sci. Technol.* **54**, 10668–10677 (2020).
14. Duan, L. et al. Efficient photocatalytic PFOA degradation over boron nitride. *Environ. Sci. Technol. Lett.* **7**, 613–619 (2020).
15. Qian, L., Kopinke, F.-D. & Georgi, A. Photodegradation of perfluorooctanesulfonic acid on Fe-zeolites in water. *Environ. Sci. Technol.* **55**, 614–622 (2021).
16. Bao, Y. et al. Degradation of PFOA substitute: GenX (HFPO–DA ammonium salt): oxidation with UV/persulfate or reduction with UV/sulfite? *Environ. Sci. Technol.* **52**, 11728–11734 (2018).
17. Qian, Y. et al. Perfluorooctanoic acid degradation using UV–persulfate process: modeling of the degradation and chlorate formation. *Environ. Sci. Technol.* **50**, 772–781 (2016).
18. Bruton, T. A. & Sedlak, D. L. Treatment of aqueous film-forming foam by heat-activated persulfate under conditions representative of in situ chemical oxidation. *Environ. Sci. Technol.* **51**, 13878–13885 (2017).
19. Duchesne, A. L. et al. Remediation of PFAS-contaminated soil and granular activated carbon by smoldering combustion. *Environ. Sci. Technol.* **54**, 12631–12640 (2020).
20. Huang, S. & Jaffé, P. R. Defluorination of perfluorooctanoic acid (PFOA) and perfluorooctane sulfonate (PFOS) by Acidimicrobium sp. Strain A6. *Environ. Sci. Technol.* **53**, 11410–11419 (2019).
21. Bentel, M. J. et al. Defluorination of per- and polyfluoroalkyl substances (PFASs) with hydrated electrons: structural dependence and implications to PFAS remediation and management. *Environ. Sci. Technol.* **53**, 3718–3728 (2019).
22. Bentel, M. J. et al. Degradation of perfluoroalkyl ether carboxylic acids with hydrated electrons: structure–reactivity relationships and environmental implications. *Environ. Sci. Technol.* **54**, 2489–2499 (2020).
23. Kim, T.-H. et al. Decomposition of perfluorooctane sulfonate (PFOS) using a hybrid process with electron beam and chemical oxidants. *Chem. Eng. J.* **361**, 1363–1370 (2019).
24. Stratton, G. R. et al. Plasma-based water treatment: efficient transformation of perfluoroalkyl substances in prepared solutions and contaminated groundwater. *Environ. Sci. Technol.* **51**, 1643–1648 (2017).
25. Singh, R. K. et al. Breakdown products from perfluorinated alkyl substances (PFAS) degradation in a plasma-based water treatment process. *Environ. Sci. Technol.* **53**, 2731–2738 (2019).
26. Lyu, X.-J., Li, W.-W., Lam, P. K. S. & Yu, H.-Q. Insights into perfluorooctane sulfonate photodegradation in a catalyst-free aqueous solution. *Sci. Rep.* **5**, 9353 (2015).
27. Park, H. et al. Reductive defluorination of aqueous perfluorinated alkyl surfactants: effects of ionic headgroup and chain length. *J. Phys. Chem. A* **113**, 690–696 (2009).
28. Vu, C. T. & Wu, T. Adsorption of short-chain perfluoroalkyl acids (PFAAs) from water/wastewater. *Environ. Sci. Water Res. Technol.* **6**, 2958–2972 (2020).
29. Gagliano, E., Sgroi, M., Falciglia, P. P., Vagliasindi, F. G. A. & Roccaro, P. Removal of poly- and perfluoroalkyl substances (PFAS) from water by adsorption: Role of PFAS chain length, effect of organic matter and challenges in adsorbent regeneration. *Water Res.* **171**, 115381 (2020).
30. Boo, C. et al. High performance nanofiltration membrane for effective removal of perfluoroalkyl substances at high water recovery. *Environ. Sci. Technol.* **52**, 7279–7288 (2018).
31. Herkert, N. J. et al. Assessing the effectiveness of point-of-use residential drinking water filters for perfluoroalkyl substances (PFASs). *Environ. Sci. Technol. Lett.* **7**, 178–184 (2020).
32. Liu, C., Hatton, J., Arnold, W. A., Simcik, M. F. & Pennell, K. D. In situ sequestration of perfluoroalkyl substances using polymer-stabilized powdered activated carbon. *Environ. Sci. Technol.* **54**, 6929–6936 (2020).
33. Xiao, X., Ulrich, B. A., Chen, B. & Higgins, C. P. Sorption of poly- and perfluoroalkyl substances (PFASs) relevant to aqueous film-forming foam (AFFF)-impacted groundwater by biochars and activated carbon. *Environ. Sci. Technol.* **51**, 6342–6351 (2017).
34. Cao, F. et al. Synthesis and application of a highly selective molecularly imprinted adsorbent based on multi-walled carbon nanotubes for selective removal of perfluorooctanoic acid. *Environ. Sci. Water Res. Technol.* **4**, 689–700 (2018).
35. McCleaf, P. et al. Removal efficiency of multiple poly- and perfluoroalkyl substances (PFASs) in drinking water using granular activated carbon (GAC) and anion exchange (AE) column tests. *Water Res.* **120**, 77–87 (2017).
36. Wang, W. et al. Adsorption behavior and mechanism of emerging perfluoro-2-propoxypropanoic acid (GenX) on activated carbons and resins. *Chem. Eng. J.* **364**, 132–138 (2019).
37. Ching, C., Klemes, M. J., Trang, B., Dichtel, W. R. & Helbling, D. E. β-Cyclodextrin polymers with different cross-linkers and ion-exchange resins exhibit variable adsorption of anionic, zwitterionic, and nonionic PFASs. *Environ. Sci. Technol.* **54**, 12693–12702 (2020).
38. Ateia, M. et al. Rapid removal of poly- and perfluorinated alkyl substances by poly(ethylenimine)-functionalized cellulose microcrystals at environmentally relevant conditions. *Environ. Sci. Technol. Lett.* **5**, 764–769 (2018).
39. Campos-Pereira, H. et al. The adsorption of per- and polyfluoroalkyl substances (PFASs) onto ferrihydrite is governed by surface charge. *Environ. Sci. Technol.* **54**, 15722–15730 (2020).
40. Zhang, Y., Zhi, Y., Liu, J. & Ghoshal, S. Sorption of perfluoroalkyl acids to fresh and aged nanoscale zerovalent iron particles. *Environ. Sci. Technol.* **52**, 6300–6308 (2018).
41. Du, Z. et al. Selective and fast adsorption of perfluorooctanesulfonate from wastewater by magnetic fluorinated vermiculite. *Environ. Sci. Technol.* **51**, 8027–8035 (2017).
42. Meng, P. et al. Superhigh adsorption of perfluorooctane sulfonate on aminated polyacrylonitrile fibers with the assistance of air bubbles. *Chem. Eng. J.* **315**, 108–114 (2017).
43. Xiang, J. et al. Thermally driven separation of perfluoroalkyl substances with high efficiency. *ACS Appl. Mater. Interfaces* **12**, 40759–40767 (2020).
44. Ali, M. et al. Capture of perfluorooctanoic acid using oil-filled graphene oxide–silica hybrid capsules. *Environ. Sci. Technol.* **54**, 3549–3558 (2020).
45. Ateia, M., Alsbaiee, A., Karanfil, T. & Dichtel, W. Efficient PFAS removal by amine-functionalized sorbents: critical review of the current literature. *Environ. Sci. Technol. Lett.* **6**, 688–695 (2019).
46. Kim, C., Lee, S. S., Lafferty, B. J., Giammar, D. E. & Fortner, J. D. Engineered superparamagnetic nanomaterials for arsenic(v) and chromium(vi) sorption and separation: quantifying the role of organic surface coatings. *Environ. Sci. Nano* **5**, 556–563 (2018).
47. Goss, K.-U. The pKa values of PFOA and other highly fluorinated carboxylic acids. *Environ. Sci. Technol.* **42**, 456–458 (2008).

48. Ji, W. et al. Removal of GenX and perfluorinated alkyl substances from water by amine-functionalized covalent organic frameworks. *J. Am. Chem. Soc.* **140**, 12677–12681 (2018).
49. Brooke, D., Footitt, A. & Nwaogu, T. *Environmental Risk Evaluation Report: Perfluorooctanesulphonate (PFOS)* (2004).
50. Burns, D. C., Ellis, D. A., Li, H., McMurdo, C. J. & Webster, E. Experimental pKa determination for perfluorooctanoic acid (PFOA) and the potential impact of pKa concentration dependence on laboratory-measured partitioning phenomena and environmental modeling. *Environ. Sci. Technol.* **42**, 9283–9288 (2008).
51. Cheng, J., Psillakis, E., Hoffmann, M. R. & Colussi, A. J. Acid dissociation versus molecular association of perfluoroalkyl oxoacids: environmental implications. *J. Phys. Chem. A* **113**, 8152–8156 (2009).
52. Park, M. et al. Adsorption of perfluoroalkyl substances (PFAS) in groundwater by granular activated carbons: Roles of hydrophobicity of PFAS and carbon characteristics. *Water Res.* **170**, 115364 (2020).
53. Sha, B. et al. Adsorption of organic amines from wastewater by carboxyl group-modified polyacrylonitrile fibers. *J. Appl. Polym. Sci.* **128**, 4124–4129 (2013).
54. Wang, L. & Song, J. Enhanced NH3 sensing properties of carboxyl functionalized carbon nanocoil. *Mater. Res. Express* **7**, 075014 (2020).
55. Fatisson, J., Domingos, R. F., Wilkinson, K. J. & Tufenkji, N. Deposition of TiO_2 nanoparticles onto silica measured using a quartz crystal microbalance with dissipation monitoring. *Langmuir* **25**, 6062–6069 (2009).
56. Quevedo, I. R., Olsson, A. L. J. & Tufenkji, N. Deposition kinetics of quantum dots and polystyrene latex nanoparticles onto alumina: role of water chemistry and particle coating. *Environ. Sci. Technol.* **47**, 2212–2220 (2013).
57. Sauerbrey, G. Verwendung von Schwingquarzen zur Wägung dünner Schichten und zur Mikrowägung. *Z. Phys.* **155**, 206–222 (1959).
58. Kim, C. & Fortner, J. D. Surface-engineered nanomaterials in water: understanding critical dynamics of soft organic coatings and relative aggregation density. *Environ. Sci. Technol.* **54**, 13548–13555 (2020).
59. Maimaiti, A. et al. Competitive adsorption of perfluoroalkyl substances on anion exchange resins in simulated AFFF-impacted groundwater. *Chem. Eng. J.* **348**, 494–502 (2018).
60. Kim, C. et al. Surface functionalized nanoscale metal oxides for arsenic(v), chromium(vi), and uranium(vi) sorption: considering single- and multi-sorbate dynamics. *Environ. Sci. Nano* **7**, 3805–3813 (2020).
61. Niu, H. & Cai, Y. Preparation of octadecyl and amino mixed group modified titanate nanotubes and its efficient adsorption to several ionic or ionizable organic analytes. *Anal. Chem.* **81**, 9913–9920 (2009).
62. Müller, S., Behrends, T. & van Genuchten, C. M. Sustaining efficient production of aqueous iron during repeated operation of Fe(0)-electrocoagulation. *Water Res.* **155**, 455–464 (2019).
63. Esfandiar, N., Suri, R. & McKenzie, E. R. Competitive sorption of Cd, Cr, Cu, Ni, Pb and Zn from stormwater runoff by five low-cost sorbents; effects of co-contaminants, humic acid, salinity and pH. *J. Hazard. Mater.* **423**, 126938 (2022).
64. Genç-Fuhrman, H., Mikkelsen, P. S. & Ledin, A. Simultaneous removal of As, Cd, Cr, Cu, Ni and Zn from stormwater using high-efficiency industrial sorbents: Effect of pH, contact time and humic acid. *Sci. Total Environ.* **566-567**, 76–85 (2016).
65. Yu, W. W., Falkner, J. C., Yavuz, C. T. & Colvin, V. L. Synthesis of monodisperse iron oxide nanocrystals by thermal decomposition of iron carboxylate salts. *Chem. Commun.* 2306–2307 (2004).
66. Prakash, A. et al. Bilayers as phase transfer agents for nanocrystals prepared in nonpolar solvents. *ACS Nano* **3**, 2139–2146 (2009).
67. Sperling, R. A. & Parak, W. J. Surface modification, functionalization and bioconjugation of colloidal inorganic nanoparticles. *Philos. Trans. R. Soc. A Math. Phys. Eng. Sci.* **368**, 1333–1383 (2010).
68. Dunér, G., Thormann, E. & Dėdinaitė, A. Quartz Crystal Microbalance with Dissipation (QCM-D) studies of the viscoelastic response from a continuously growing grafted polyelectrolyte layer. *J. Colloid Interface Sci.* **408**, 229–234 (2013).
69. Rattanaoudom, R., Visvanathan, C. & Boontanon, S. K. Removal of concentrated PFOS and PFOA in synthetic industrial wastewater by powder activated carbon and hydrotalcite. *J. Water Sustain* **2**, 245–258 (2012).
70. Deng, S. et al. Enhanced adsorption of perfluorooctane sulfonate and perfluorooctanoate by bamboo-derived granular activated carbon. *J. Hazard. Mater.* **282**, 150–157 (2015).
71. Chen, W., Zhang, X., Mamadiev, M. & Wang, Z. Sorption of perfluorooctane sulfonate and perfluorooctanoate on polyacrylonitrile fiber-derived activated carbon fibers: in comparison with activated carbon. *RSC Adv.* **7**, 927–938 (2017).
72. Wang, B. et al. Covalent triazine-based framework: a promising adsorbent for removal of perfluoroalkyl acids from aqueous solution. *Environ. Pollut.* **216**, 884–892 (2016).
73. Yu, Q., Zhang, R., Deng, S., Huang, J. & Yu, G. Sorption of perfluorooctane sulfonate and perfluorooctanoate on activated carbons and resin: kinetic and isotherm study. *Water Res.* **43**, 1150–1158 (2009).
74. Xu, C., Chen, H. & Jiang, F. Adsorption of perflourooctane sulfonate (PFOS) and perfluorooctanoate (PFOA) on polyaniline nanotubes. *Colloids Surf. A Physicochem. Eng. Asp.* **479**, 60–67 (2015).
75. Deng, S. et al. Highly efficient sorption of perfluorooctane sulfonate and perfluorooctanoate on a quaternized cotton prepared by atom transfer radical polymerization. *Chem. Eng. J.* **193–194**, 154–160 (2012).
76. Deng, S. et al. Adsorption of perfluorinated compounds on aminated rice husk prepared by atom transfer radical polymerization. *Chemosphere* **91**, 124–130 (2013).
77. Chen, M.-J. et al. Influence of crystal topology and interior surface functionality of metal-organic frameworks on PFOA sorption performance. *Microporous Mesoporous Mater.* **236**, 202–210 (2016).
78. Gong, Y., Wang, L., Liu, J., Tang, J. & Zhao, D. Removal of aqueous perfluorooctanoic acid (PFOA) using starch-stabilized magnetite nanoparticles. *Sci. Total Environ.* **562**, 191–200 (2016).
79. Chen, X., Xia, X., Wang, X., Qiao, J. & Chen, H. A comparative study on sorption of perfluorooctane sulfonate (PFOS) by chars, ash and carbon nanotubes. *Chemosphere* **83**, 1313–1319 (2011).
80. Gao, Y., Deng, S., Du, Z., Liu, K. & Yu, G. Adsorptive removal of emerging polyfluoroalky substances F-53B and PFOS by anion-exchange resin: a comparative study. *J. Hazard. Mater.* **323**, 550–557 (2017).
81. Deng, S., Yu, Q., Huang, J. & Yu, G. Removal of perfluorooctane sulfonate from wastewater by anion exchange resins: effects of resin properties and solution chemistry. *Water Res.* **44**, 5188–5195 (2010).
82. Yu, Q., Deng, S. & Yu, G. Selective removal of perfluorooctane sulfonate from aqueous solution using chitosan-based molecularly imprinted polymer adsorbents. *Water Res.* **42**, 3089–3097 (2008).
83. Zhang, Q., Deng, S., Yu, G. & Huang, J. Removal of perfluorooctane sulfonate from aqueous solution by crosslinked chitosan beads: sorption kinetics and uptake mechanism. *Bioresour. Technol.* **102**, 2265–2271 (2011).
84. Luo, Q., Zhao, C., Liu, G. & Ren, H. A porous aromatic framework constructed from benzene rings has a high adsorption capacity for perfluorooctane sulfonate. *Sci. Rep.* **6**, 20311 (2016).

ACKNOWLEDGEMENTS

This work was supported by the Strategic Environmental Research and Development Program (SERDP) funding under contract W912HQ-18-C0002 "Development of Coupled Physiochemical and Biological Systems for In-Situ Remediation of Mixed Perfluorinated Chemical and Chlorinated Solvent Groundwater Plumes (ER-2714)" and the US NSF Engineering Research Center Nanotechnology-Enabled Water Treatment (NEWT) #EEC-1449500. The contents of this manuscript have not been subject to agency review and do not necessarily represent the views of the sponsoring agency. This work was also supported by GIST Research Institute (GRI) grant funded by the GIST in 2023. ICP-MS and TOC analysis were provided by the Yale Analytical and Stable Isotope Center (YASIC) while TEM access was provided by Yale Institute for Nanoscience and Quantum Engineering (YINQ) at Yale University.

AUTHOR CONTRIBUTIONS

J.L. designed and performed experiments, analyzed data, wrote and edited the manuscript. C.K. designed experiments, analyzed data, and edited the manuscript. C.L. conducted column experiments and analyzed data. M.S.W. reviewed and edited the manuscript. N.L.C. reviewed and edited the manuscript. K.D.P. wrote, reviewed, and edited the manuscript. J.D.F. designed and supervise the research work, wrote and edited the manuscript. All authors read and approved the final manuscript.

COMPETING INTERESTS

The authors declare no competing interests.

ADDITIONAL INFORMATION

Supplementary information The online version contains supplementary material available at https://doi.org/10.1038/s41545-023-00263-9.

Correspondence and requests for materials should be addressed to John D. Fortner.

Reprints and permission information is available at http://www.nature.com/reprints

Publisher's note Springer Nature remains neutral with regard to jurisdictional claims in published maps and institutional affiliations.